Pulse Sequence based Multi-acquisition MR Intensity Normalization

Amod Jog, **Snehashis Roy**, **Aaron Carass**, and **Jerry L. Prince**
Image Analysis and Communications Laboratory, The Johns Hopkins University, Baltimore, MD, USA

Abstract

Intensity normalization is an important preprocessing step in magnetic resonance (MR) image analysis. In MR images (MRI), the observed intensities are primarily dependent on (1) intrinsic magnetic resonance properties of the tissues such as proton density (P_D), longitudinal and transverse relaxation times (T_1 and T_2 respectively), and (2) the scanner imaging parameters like echo time (TE), repeat time (TR), and flip angle (a). We propose a method which utilizes three co-registered images with different contrast mechanisms (PD-weighted, T2-weighted and T1-weighted) to first estimate the imaging parameters and then estimate P_D, T_1, and T_2 values. We then normalize the subject intensities to a reference by simply applying the pulse sequence equation of the reference image to the subject tissue parameters. Previous approaches to solve this problem have primarily focused on matching the intensity histograms of the subject image to a reference histogram by different methods. The fundamental drawback of these methods is their failure to respect the underlying imaging physics and tissue biology. Our method is validated on phantoms and we show improvement of normalization on real images of human brains.

Keywords

intensity normalization/standardization; brain; magnetic resonance imaging; pulse sequence

1. INTRODUCTION

MRI is one of the principal modalities used in imaging brain tissue. Brain MRI scans are collected on many different scanners and at many different sites. The quality of these images is highly dependent on the imaging parameters and the calibration of the scanners, the variations of which lead to vastly differing intensity profiles for images. It is a fundamental problem of MR imaging that the image voxel intensities do not have any specific numeric meaning, unlike computed tomography (CT). The performance of image analysis routines like segmentation and registration is dependent on the underlying intensity distribution,[1] which can be made consistent through intensity normalization or standardization. Previous work,[1-8] focuses primarily on histogram matching. Histogram matching however suffers from quantization artifacts. Additionally, forcing a subject image histogram to match a reference, forces the tissue intensity distribution of the subject to be equal to that of the reference. This can have unwanted consequences if the subject and the reference brain anatomies differ by a lot. Landmark-based approaches like [1,3,4,9] result in using linear,[4] piece-wise linear[1,9] or polynomial[3] intensity transforms calculated from landmarks on intensity histograms. These types of one-to-one transforms are insufficient to model the highly nonlinear variations introduced in different images by the MR imaging physics.

Further author information: Send correspondence to Amod Jog amod@cs.jhu.edu.

Recent work by Weisenfeld *et al.*[5] and Jäger *et al.*[10] uses multiple images and focuses on matching multidimensional histograms of the subject and the reference. Though these methods can result in a nonlinear, many-to-many transform, the basic issue of forcing the subject joint histogram to match a reference joint histogram remains.

All the above mentioned methods overlook a vital point while performing intensity normalization, the MR imaging physics and its effect on tissue biology. The contrast obtained in an MR image is dependent on imaging parameters like repetition time *TR*, single or multiple echo times *TE*'s, and flip angle a. It is also dependent on the physical properties of the underlying tissue such as the proton density P_D, and the longitudinal and transverse relaxation times, T_1 and T_2 respectively. We propose to use the imaging equations of the pulse sequences in our data to estimate the aforementioned imaging parameters. Using these, we intend to use multiple different images obtained by different pulse sequences to estimate the intrinsic biophysical properties $\beta = [P_D, T_1, T_2]$. Normalization entails simply applying the reference pulse sequence equations, on the subject β properties to generate new intensities. We show that this approach is feasible using the highly nonlinear pulse sequence equations and also describe a better performing algorithm using approximations of the actual pulse sequence equations. This approach shares its principle with a segmentation approach described by Fischl *et al.*[7] Sec. 2 describes our assumptions and the main algorithm. Sec. 3 describes our results using phantom as well as real data. We describe future avenues of work and conclusions in Sec. 4.

2. METHOD

Consider a set of co-registered subject images $\mathscr{S} = \{S_1, S_2, S_3\}$, which we intend to normalize using a set of co-registered reference images, $\mathscr{R} = \{R_1, R_2, R_3\}$. Each S_i, as well as the corresponding R_i, is produced by a pulse sequence Γ_i. In our case, Γ_1 and Γ_2 denote the P_D-weighted (P_D-w) and T_2-weighted (T_2-w) outputs of a double spin echo sequence, respectively. Γ_3 denotes T_1-weighted (T_1-w) spoiled gradient recalled echo (SPGR) sequence. The goal is to normalize S_3 to R_3 with the help of the other two acquisitions. Fig. 1 shows the three input images. These sequences use imaging parameters like repetition time (*TR*), echo time (*TE*), flip angle (a) and a scalar gain (*A*). Let the set of imaging parameters of Γ_i for the subject be denoted as Θ_{S_i}, $i \in \{1, 2, 3\}$. In our case, for the double spin echo sequences Γ_1 and Γ_2, $\Theta_{S_i} = \{TR_i, TE_{1i}, TE_{2i}, A_i\}$, $i \in 1, 2$. For the T_1-w SPGR sequence Γ_3, $\Theta_{S_3} = \{TR_3, TE_3, a_3, A_3\}$. We also denote the intrinsic tissue MR properties at a voxel location **x** in the subject as $\beta(\mathbf{x}) = [P_D(\mathbf{x}), T_1(\mathbf{x}), T_2(\mathbf{x})]$. The set of imaging parameters for reference images R_i is denoted by Θ_{R_i}. To keep the notation compact, we refrain from using the subscripts "S" and "R" in the parameter names TR_i, TE_i a_i, and A_i. Instead we will refer to their collection using Θ_{S_i} for the subject and Θ_{R_i} for the reference, where $i \in \{1, 2, 3\}$. Using this notation, we can describe the intensity at a voxel **x** in the subject image for a sequence Θ_i with imaging parameters Θ_{S_i} in Eq. (1).

$$S_i(\mathbf{x}) = \Gamma_i\left(\beta(\mathbf{x}); \Theta_{S_i}\right) \quad (1)$$

The human brain tissue primarily consists of three major tissue classes, cerebrospinal uid (CSF), gray matter (GM) and white matter (WM). We assume that the mean β values for these three major tissues are known for 1.5T scanners,[13] as $\bar{\beta}_C = [1.00, 2650, 329]$, $\bar{\beta}_G = [0.86, 833, 83]$, and $\bar{\beta}_W = [0.73, 500, 70]$, respectively. T_1 and T_2 are in milliseconds while P_D is relative. Additionally, for a subject image S_i generated by the pulse sequence Γ_i, $i \in \{1, 2, 3\}$, let $\bar{s}_{C,i}$, $\bar{s}_{G,i}$, and $\bar{s}_{W,i}$ represent the mean intensities of CSF, GM, and WM

respectively. Our key assumption is that the mean tissue β values give rise the mean tissue intensities when the imaging equation for Γ_i is applied.

2.1 Normalization Algorithm

(a) Estimating Θ_{S_i} and Θ_{R_i}—Our key assumption is that for a pulse sequence Γ_i, the average MR tissue properties *i.e.* $\bar{\beta}_C$, $\bar{\beta}_G$, and $\bar{\beta}_W$ give rise to the average tissue intensities $\bar{s}_{C,i}$, $\bar{s}_{G,i}$, and $\bar{s}_{W,i}$ respectively. This is represented as,

$$\Gamma_i\left(\bar{\beta}_C;\Theta_{S_i}\right)=\bar{s}_{C,i}, \quad \Gamma_i\left(\bar{\beta}_G;\Theta_{S_i}\right)=\bar{s}_{G,i} \quad \Gamma_i\left(\bar{\beta}_W;\Theta_{S_i}\right)=\bar{s}_{W,i}. \quad (2)$$

We solve this system to estimate Θ_{S_i} and a corresponding equivalent system for the reference set to estimate Θ_{R_i}. Since we have three equations, in principle we can solve this system if Θ_{S_i} has three or fewer parameters. We denote $\widehat{\Theta}_{S_i}$ as the estimate of Θ_{S_i}, $i \in \{1, 2, 3\}$ which we get as a solution. We also estimate $\widehat{\Theta}_{R_i} i \in \{1, 2, 3\}$ for the reference images in an analogous fashion.

(b) Estimating β(x)—We know the relationship between β(**x**) and the recorded intensity from Eq. 1. For a particular subject voxel **x**, we have three intensities $s_i(\mathbf{x})$, $i \in \{1, 2, 3\}$ from the three images. Thus we have a system of equations to solve for β(**x**) in Eq. 3

$$\Gamma_1\left(\beta\left(\mathbf{x}\right);\widehat{\Theta}_{S_1}\right)=s_1\left(\mathbf{x}\right), \quad \Gamma_2\left(\beta\left(\mathbf{x}\right);\widehat{\Theta}_{S_2}\right)=s_2\left(\mathbf{x}\right), \quad \Gamma_3\left(\beta\left(\mathbf{x}\right);\widehat{\Theta}_{S_3}\right)=s_3\left(\mathbf{x}\right), \quad (3)$$

This system has three equations and three unknowns since $\beta = [P_D, T_1, T_2]$. So in principle it can be solved to estimate β(**x**); $\forall \mathbf{x}$ in the subject image. Let $\widehat{\beta}\left(\mathbf{x}\right)$ be the solution estimate of β(**x**).

(c) Applying Reference Pulse Sequence—To normalize voxel intensities of subject image S_3 to the reference image R_3, we only have to apply the pulse sequence Γ_3 using imaging parameters $\widehat{\Theta}_{R_3}$ estimated in (a) to $\widehat{\beta}\left(\mathbf{x}\right)$ estimated in (b) to generate a normalized subject image $S_3^{(n)}$.

$$S_3^{(n)}\left(\mathbf{x}\right)=\Gamma_3\left(\beta\left(\mathbf{x}\right);\widehat{\Theta}_{R_3}\right). \quad (4)$$

In essence, we are extracting the subject's biology and applying the reference's imaging physics to generate a subject image as it would have looked, had we imaged it with the same pulse sequence parameters as that of the reference. We have described here a general algorithm to normalize S_3 to R_3. The implementation of this algorithm depends on how Γ_i is modeled. We describe two ways of using this algorithm. The first one (denoted by M1), described in Sec. 2.2 uses the actual pulse sequence equations derived for the sequences we have used.[12] We show that this approach is feasible subject to certain assumptions. Despite its feasibility, M1 has its limitations, which are reected in its performance. In Sec. 2.3 we describe an approach, M2, where Γ_i are modeled as approximate forms of the imaging equations used in M1.

2.2 Using Exact Imaging Equations: M1

For each S_i, we use the imaging equations described in[12] directly. Eqns. 5, 6, 7 describe the Γ_i we use in this approach.

$$S_1(\mathbf{x}) = \Gamma_1\left(\beta(\mathbf{x});\Theta_{S_1}\right) = A_1 P_D(\mathbf{x})\left(1 - 2e^{-\frac{TR_1 - \frac{TE_{11}+TE_{21}}{2}}{T_1(\mathbf{x})}} + 2e^{-\frac{TR_1 - \frac{TE_{11}}{2}}{T_1(\mathbf{x})}} - e^{-\frac{TR_1}{T_1(\mathbf{x})}}\right) e^{-\frac{TE_{11}}{T_2(\mathbf{x})}} \quad (5)$$

$$S_2(\mathbf{x}) = \Gamma_2\left(\beta(\mathbf{x});\Theta_{S_2}\right) = A_2 P_D(\mathbf{x})\left(1 - 2e^{-\frac{TR_2 - \frac{TE_{12}+TE_{22}}{2}}{T_1(\mathbf{x})}} + 2e^{-\frac{TR_2 - \frac{TE_{12}}{2}}{T_1(\mathbf{x})}} - e^{-\frac{TR_2}{T_1(\mathbf{x})}}\right) e^{-\frac{TE_{22}}{T_2(\mathbf{x})}}. \quad (6)$$

$$S_3(\mathbf{x}) = \Gamma_3\left(\beta(\mathbf{x});\Theta_{S_3}\right) = A_3 P_D(\mathbf{x})\sin\ \alpha_3\left(\frac{1 - e^{-\frac{TR_3}{T_1(\mathbf{x})}}}{1 - \cos\ \alpha_3 e^{-\frac{TR_3}{T_1(\mathbf{x})}}}\right) e^{-\frac{TE_3}{T_2^*(\mathbf{x})}}, \quad (7)$$

Here, the imaging parameters are $\Theta_{S_i} = [TR_i, TE_{i1}, TE_{i2}, A_i]$ for $i \in \{1, 2\}$ and $\Theta S_i = [TR_i, TE_i, a_i, A_i]$ for $i = 3$ where TR_i are repeat times, TE_i are echo times, A_i are scalar factors and a_i are flip angles. Note that there are four unknowns in Θ_{S_i} and as described in Sec. 2.1, we can estimate Θ_{S_i} only if we have three unknowns. To simplify, we constrain the parameters which are least variable while acquiring images in practice. Specifically for our dataset, we use $TR_3 = 15$ ms in Θ_{S_3}, $TE_{11} = 17$ ms, and $TE_{22} = 80$ ms in Θ_{S_1} and Θ_{S2}, respectively. We also approximate T_2^* in Eq. 7 by $\frac{1}{T_2^*} = \frac{1}{T_2} + k$, where k is estimated to be 0.02 for CSF using values observed in the literature.[13] We solve the equations as shown in Eq. 2 to estimate $\widehat{\Theta}_{S_i}$ and $\widehat{\beta}(\mathbf{x})$ using Newton's nonlinear least squares method. The reference pulse sequence is next applied to the estimated $\widehat{\beta}(\mathbf{x})$ to produce a normalized $S_3^{(n)}$ as per Eq. 4. Figs. 2(d)-(f) show the maps of P_D, T_2 and T_1 values produced by this method.

2.3 Solving Approximate Imaging Equations: M2

The method described in Sec. 2.2, although being the theoretically correct way, leads to non-convergent solutions, especially for CSF voxels. This can be attributed to the highly non-linear nature of the pulse sequence equations, imperfect T_2^* approximation, assumptions on one of the imaging parameters or low signal-to-noise ratio in the CSF intensities in P_D-w and T_2-w images. The average T_2^* value of CSF is considerably different from its average T_2 value, unlike GM and WM, which leads to another problem, the estimation of k. It is also computationally expensive since the nonlinear simultaneous system of equations is to be solved for each voxel. To address these issues, we approximated the pulse sequence equations by a first order Taylor series approximation, that does not need any information about the pulse sequence parameters.

Eqn. 7 is simplified using the fact that TR_3 is usually smaller than the T_1 for all the tissues,

$$\begin{aligned} \log\ S_3(\mathbf{x}) &= \log A_3 + \log P_D(\mathbf{x}) + \log\left(1 - e^{-\frac{TR_3}{T_1(\mathbf{x})}}\right) - \log\left(1 - \cos\alpha_3 e^{-\frac{TR_3}{T_1(\mathbf{x})}}\right) - \frac{TE_3}{T_2(\mathbf{x})}, \\ &\approx \theta_{31} + \log P_D(\mathbf{x}) + \frac{\theta_{32}}{T_1(\mathbf{x})} - \frac{\Theta_{33}}{T_2(\mathbf{x})}, \end{aligned} \quad (8)$$

where $\Theta_{S3} = \{\theta_{31}, \theta_{32}, \theta_{33}\}$. This is a first order approximation assuming $TR_3 < T_1(\mathbf{x}), \forall x$. Any residual part of the approximation is absorbed into the additive constant θ_{31}. This additive term also absorbs any differences in T_2 and T_2^*. Thus we model Γ_1 as in Eqn. 9.

$$\log \quad S_3(\mathbf{x}) = \log \quad \Gamma_3\left(\beta(\mathbf{x}), \Theta_{S_3}\right) = \theta_{31} + \log \quad P_D(\mathbf{x}) + \frac{\theta_{32}}{T_1(\mathbf{x})} - \frac{\theta_{33}}{T_2(\mathbf{x})} \quad (9)$$

To approximate the P_D-w and T_2-w imaging equations, we follow a slightly different strategy. In these sequences, the repetition times, TR_1, $TR_2 \approx 2000$ms, which is comparable to the T_1's of CSF. Thus we cannot use the same approximation used for SPGR. Using the fact that TE_{11} and TE_{22} are small compared to TR_1 and TR_2, we can approximate Eqn. 5-Eqn. 6 as,

$$\log \quad S_1(\mathbf{x}) = \log \quad A_1 + \log \quad P_D(\mathbf{x}) + \log\left(1 - 2e^{TR_1 - \frac{TE_{11} + TE_{21}}{2}}_{T_1(\mathbf{x})} + 2e^{-\frac{TR_1 - \frac{TE_{11}}{2}}{T_1(\mathbf{x})}} - e^{-\frac{TR_1}{T_1(\mathbf{x})}}\right) - \frac{TE_{11}}{T_2(\mathbf{x})},$$
$$\approx \quad \log \quad A_1 + \log \quad P_D(\mathbf{x}) + \log\left(1 - e^{-\frac{TR_1}{T_1(\mathbf{x})}}\right) - \frac{TE_{11}}{T_2(\mathbf{x})}. \quad (10)$$

The middle term, $\log\left(1 - e^{-\frac{TR_1}{T_1(\mathbf{x})}}\right)$, is a sharply decreasing function of $T_1(\mathbf{x})$, We can approximate it with a linearly decreasing function in $T_1(\mathbf{x})$ within the range of values that we are interested in (*i.e.* $T_1 \in (0, 6000)$ ms in the human brain at 1.5T). Thus we can write a more compact form of the approximations in Eqns. 11 12

$$\log \quad S_1(\mathbf{x}) = \log \quad \Gamma_1\left(\beta(\mathbf{x}); \Theta_{S_1}\right) = \theta_{11} + \log \quad P_D(\mathbf{x}) + \theta_{12}T_1(\mathbf{x}) - \frac{\theta_{13}}{T_2(\mathbf{x})}, \quad (11)$$

$$\log \quad S_2(\mathbf{x}) = \log \quad \Gamma_2\left(\beta(\mathbf{x}); \Theta_{S_2}\right) = \theta_{21} + \log \quad P_D(\mathbf{x}) + \theta_{22}T_1(\mathbf{x}) - \frac{\theta_{23}}{T_2(\mathbf{x})}, \quad (12)$$

where $\Theta_{S_i} = \{\theta_{i1}, \theta_{i2}, \theta_{i3}\}$, $i \in \{1, 2\}$.

Thus we have Γ_1 modeled in Eqn. 11, Γ_2 in Eqn. 12 and Γ_3 in Eqn. 9. We carry out the steps described in Sec. 2.1(a) to estimate $\widehat{\Theta}_{S_i}$ and $\widehat{\Theta}_{R_i}$. Next, we estimate $\widehat{\beta}(\mathbf{x})$. This step is easier and faster as it involves solving a quadratic equation. Thus, this approach does not face convergence issues. Normalization is as described in Sec. 2.1(c).

3. RESULTS

We performed two sets of experiments, with phantom and real images respectively. To show the biological correctness of our procedure we used simulated images with known imaging parameters from Brainweb[13] where we know the ground truth for tissue classes at each voxel and the mean values of $\overline{\beta}_C$, $\overline{\beta}_G$, and $\overline{\beta}_W$.

3.1 Brainweb Phantom Experiments

For this experiment, we used a number of simulated T_1-w SPGR images of the normal anatomical model with varying TR_3, TE_3 and flip angles α_3 and 0% noise. For reference images we used a simulated P_D-w image R_1 and a T_2-w image R_2 with $TR_1 = TR_2 = 3000$ms, $TE_{11} = TE_{21} = 17$ms and $TE_{12} = TE_{22} = 80$ms. We fixed the SPGR as the reference image, R_3, with $TR_3 = 15$ ms, $TE_3 = 2$ms, and $\alpha_3 = 30°$. Fig. 3 shows the normalization result for the given reference and a subject image with $TR_3 = 100$ms, $TE_3 = 2$ms, and $\alpha_3 = 30°$. The scale factor (A) is different for all the simulated images. The reference images are shown in Fig. 2(a)-(c) and served as the reference set of images $\mathscr{R} = \{R_1, R_2, R_3\}$. For the subject set,

$\mathscr{S} = \{S_1, S_2, S_3\}$, we set $S_1 = R_1$ and $S_2 = R_2$. S_3 is chosen to vary with T_R, T_E, and α. Since all the images come from a single subject with common biological properties, a perfect normalization scheme will convert the subject SPGR image into an exact replica of the reference SPGR image. We measured image similarity between the reference and the normalized subject image using metrics like mean squared error (MSE) in Table 1, visual information fidelity (VIF)[14] in Table 2. We compared M1 and M2, with histogram matching (HM), white matter peak scaling (WMP),[4] and a landmark-based method piece-wise linear method (UPL).[1] VIF is an image quality metric based on the perception of the human visual system of comparing two images. A value equal to 1 indicates visually identical images. We also tested the similarity between the reference and normalized subject image histograms by calculating the Kullback-Leibler (KL) distance. Results are shown in Table 3. Since KL distance is asymmetric, we calculated KL(subject, ref) for all cases.

3.2 Real Data Experiments

To test our methods on real image data, we chose to use the Baltimore Longitudinal Study of Aging (BLSA).[15] For nine subjects, we chose two consecutive scans per subject. In general these scans are a year apart of each other. We assume that the anatomical change in the brain is negligible within these two scans, as the subjects are healthy. The SPGR images are $0.9375 \times 0.9375 \times 1.5$ mm^3 in resolution while the P_D-w and T_2-w images are of $0.9375 \times 0.9375 \times 5$ mm^3 resolution. Initial preprocessing involved isotropic resampling, removal of non-brain tissue using SPECTRE,[16] removing intensity inhomogeneities using N3,[17] affine registration of the P_D-w and T_2-w images to the corresponding SPGR. The second year images were affine registered to the first, so as to carry out pixel-wise comparisons between the two. Table 4 describes the average MSE and KL distances between year one and normalized year two scan across all subjects. WMP and M2 are comparable since the pulse sequence used in both years is identical with possibly only a scale difference in the intensities. Fig. 4 shows the normalization result on a sample year 1 - year 2 pair of images.

4. CONCLUSIONS AND FUTURE WORK

We have presented a novel paradigm for performing intensity normalization, which stays true to the underlying intrinsic biological MR properties. We have validated its performance using phantom and real brain images. An additional benefit of this method is the ability to characterize complex pulse sequences using three parameter pulse sequence approximate equations. Estimation of the tissue properties allows us to synthesize any desired MR contrast. This opens up avenues into the design of optimal pulse sequences for the best tissue contrast as well. We are interested in characterizing the underlying biological parameter space and reducing the number of images required, so that this approach can be applied more generally.
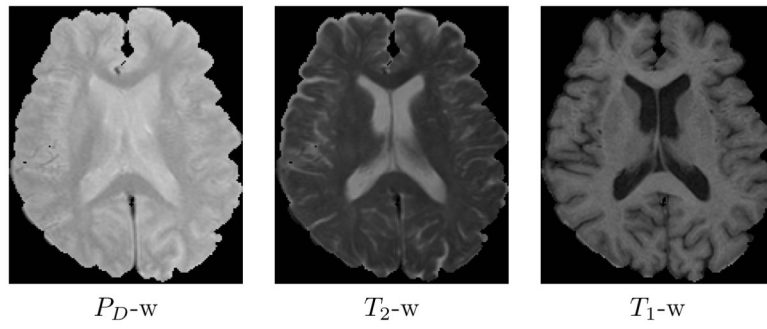
Acknowledgments

REFERENCES

[1]. Nyúl LG, Udupa JK. On standardizing the MR image intensity scale. Mag. Reson. Med. 1999; 42(6):1072–1081.

[2]. Roy, S.; Carass, A.; Prince, JL. A Compressed Sensing Approach For MR Tissue Contrast Synthesis; [22nd Conf. on Inf. Proc. in Medical Imaging (IPMI 2011)]; 2011; p. 371-383.
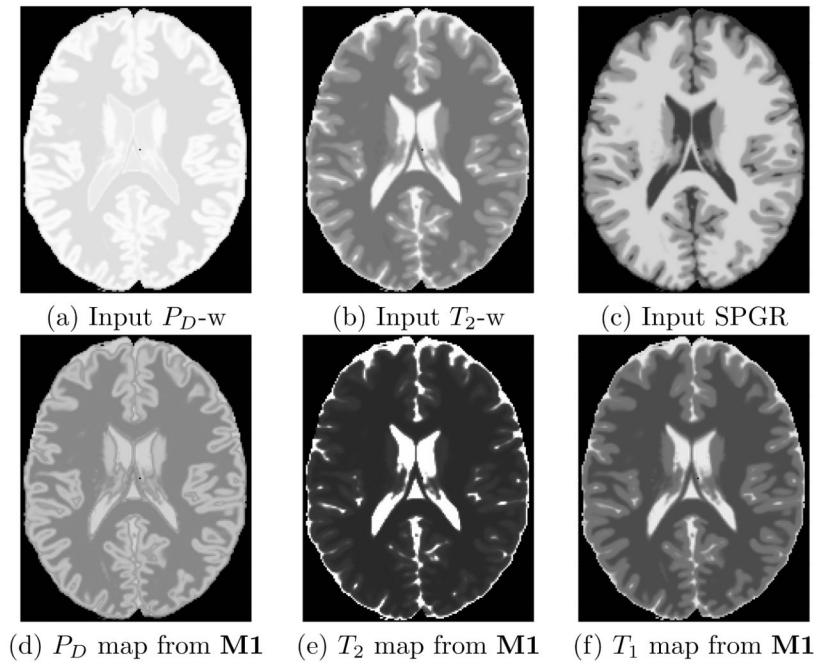
[3]. Hellier P. Consistent intensity correction of MR images. [IEEE Intl. Conf. on Image Proc.]. 1:1109–1112.

[4]. Christensen JD. Normalization of brain magnetic resonance images using histogram even-order derivative analysis. Mag. Reson. Imag. 2003; 21(7):817–820.

[5]. Weisenfeld NI, Warfield SK. Normalization of joint image-intensity statistics in MRI using the Kullback-Leibler divergence. [IEEE Intl. Symp. on Biomed. Imaging]. 2004; 1:101–104.

[6]. Jäger F, Hornegger J. Nonrigid Registration of Joint Histograms for Intensity Standardization in Magnetic Resonance Imaging. IEEE Trans. Med. Imag. 2009; 28(1):137–150.

[7]. Fischl B, Salat DH, van der Kouwe AJW, Makris N, Segonne F, Quinn BT, Dale AM. Sequence-independent segmentation of magnetic resonance images. NeuroImage. 2004; 23(S1):S69–S84. [PubMed: 15501102]

[8]. Wang L, Lai H-M, Barker GJ, Miller DH, Tofts PS. Correction for variations in mri scanner sensitivity in brain studies with histogram matching. Mag. Reson. Med. 1998; 39(2):322–327.

[9]. Robitaille N, Mouiha A, Crépeault B, Valdivia F, Duchesne S, The Alzheimer's Disease Neuroimaging Initiative. Tissue-Based MRI Intensity Standardization: Application to Multicentric Datasets. Intl. Journal of Biomed. Imag. 2012:2012.

[10]. Jäger, F.; Nyúl, L.; Frericks, B.; Wacker, F.; Hornegger, J. [Whole Body MRI Intensity Standardization]. Springer; 2007.

[11]. Bezdek JC. A Convergence Theorem for the Fuzzy ISO-DATA Clustering Algorithms. IEEE Trans. on Pattern Anal. Machine Intell. 1980; 20(1):1–8.

[12]. Glover, GH. [Handbook of MRI Pulse Sequences]. Vol. 18. Elsevier Academic Press; 2004.

[13]. Kwan RKS, Evans AC, Pike GB. MRI simulation-based evaluation of image-processing and classification methods. IEEE Trans. Med. Imag. 1999; 18(11):1085–1097.

[14]. Sheikh HR, Bovik AC. A visual information fidelity approach to video quality assessment. [Intl. Workshop on Video Processing and Quality Metrics for Consumer Electronics]. 2005:23–25.

[15]. Resnick SM, Goldszal AF, Davatzikos C, Golski S, Kraut MA, Metter EJ, Bryan RN, Zonderman AB. One-year Age Changes in MRI Brain Volumes in Older Adults. Cerebral Cortex. 2000; 10(5):464–472. [PubMed: 10847596]

[16]. Carass A, Cuzzocreo J, Wheeler MB, Bazin P-L, Resnick SM, Prince JL. Simple Paradigm for Extra-cerebral Tissue Temoval: Algorithm and Analysis. NeuroImage. 2011; 56(4):1982–1992. [PubMed: 21458576]

[17]. Sled JG, Zijdenbos AP, Evans AC. A nonparametric method for automatic correction of intensity nonuniformity in MRI data. IEEE Trans. Med. Imag. Feb.1998 17:87–97.

P_D-w $\qquad\qquad$ T_2-w $\qquad\qquad$ T_1-w

Figure 1.
Example input images

(a) Input P_D-w   (b) Input T_2-w   (c) Input SPGR

(d) P_D map from **M1**   (e) T_2 map from **M1**   (f) T_1 map from **M1**
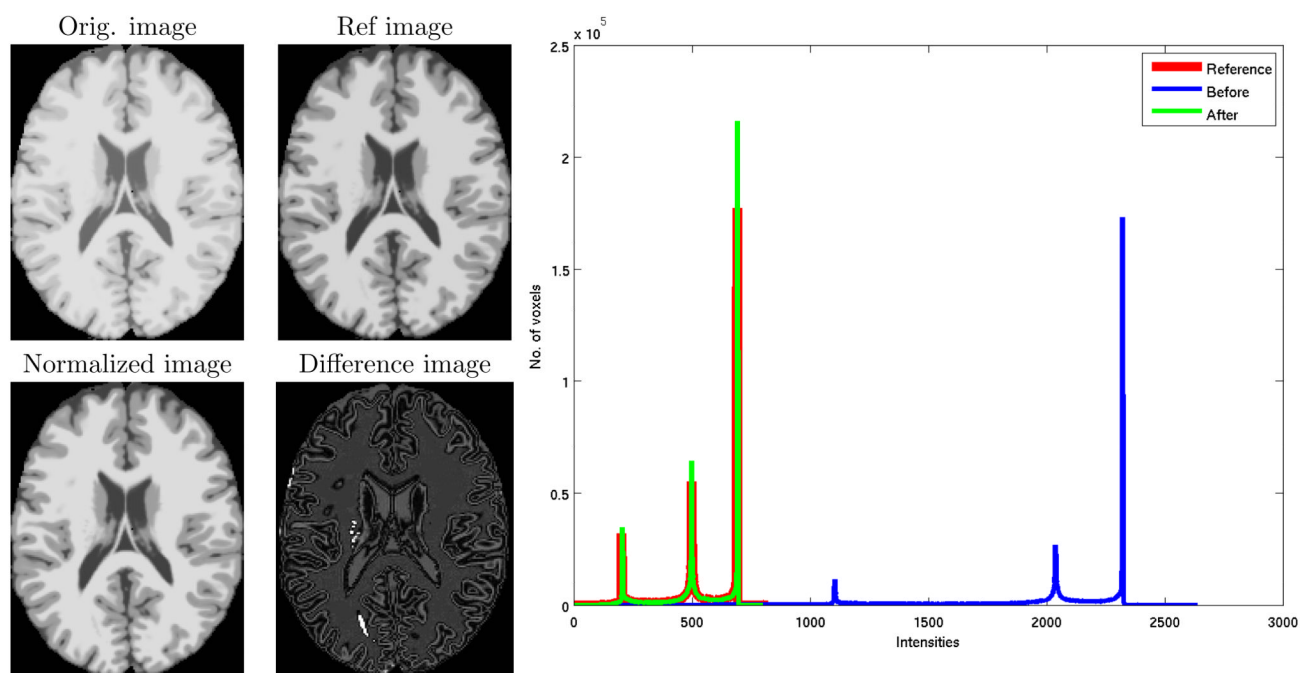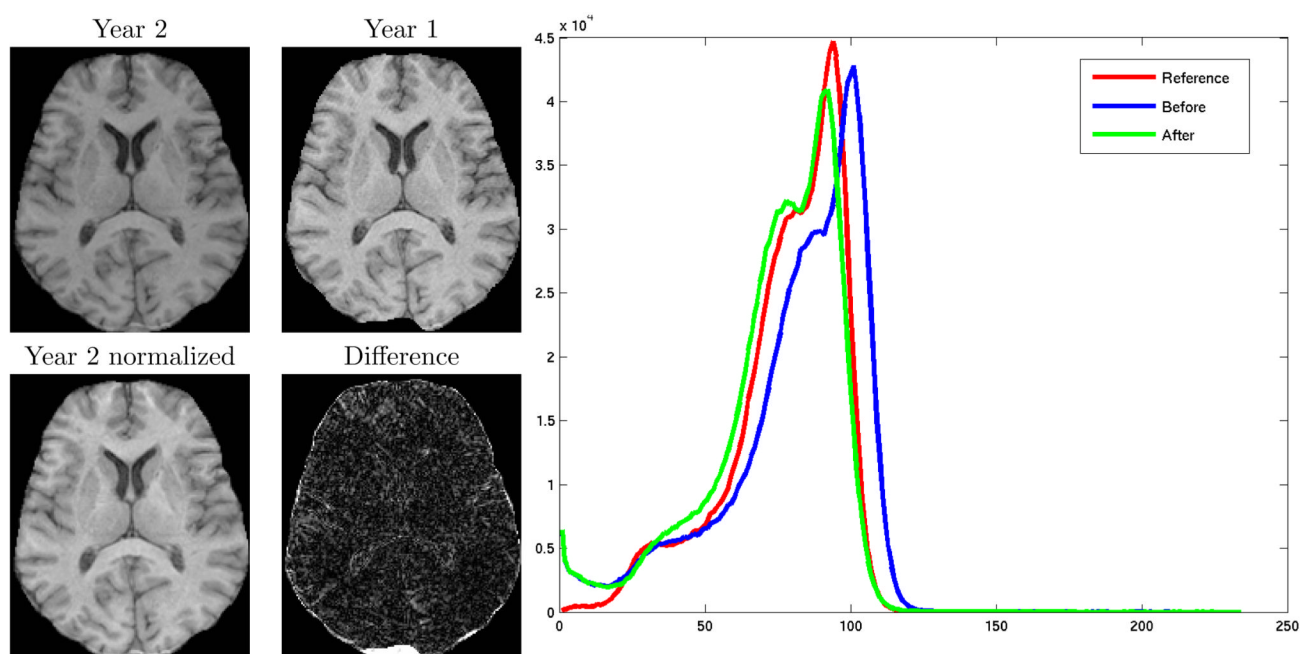
Figure 2.
Estimated β maps for a Brainweb phantom using M1 (2nd row)

Figure 3.
Normalization of Brainweb phantom with M2

Figure 4.
Normalizing year 2 image to a year 1 image using M2. We show the difference image between the normalized year 2 image and the year 1 image along with the histograms on the right.

Table 1

MSE values after normalizing with different methods.

$\begin{bmatrix} T_R & T_E & a \end{bmatrix}$	Before	HM	WMP	UPL	MI	M2
[15 2 60]	17549.0	4378.0	93.4	1.026	3.833	**0.343**
[100 2 30]	590250.0	537170.0	1868.5	3830.5	83.17	**1.878**
[15 10 30]	1082.6	493.5	7.371	**3.002**	122.48	3.712
[15 2 90]	36790.0	3.15	132.35	1.375	5.813	**0.525**
[30 2 30]	43766.0	35597.0	108.93	1.318	6.938	**0.227**

Table 2

VIF values after normalizing with different methods.

$\begin{bmatrix} T_R & T_E & a \end{bmatrix}$	Before	HM	WMP	UPL	MI	M2
[15 2 60]	0.7496	0.2382	0.8259	**0.9824**	0.9537	0.9802
[100 2 30]	0.5638	0.2231	0.5206	0.3277	0.7820	**0.9255**
[15 10 30]	0.8782	0.4711	0.8976	**0.9488**	0.8983	0.9322
[15 2 90]	0.6538	0.9601	0.7988	**0.9782**	0.9405	0.9721
[30 2 30]	0.8524	0.2816	0.8057	0.9796	0.9462	**0.9854**

Table 3

KL values after normalizing with different methods (smaller the value, closer the fit)

$[T_R \quad T_E \quad a]$	HM	WMP	UPL	MI	M2
[15 2 60]	0.8331	0.6233	0.0844	0.0061	**0.0007**
[100 2 30]	0.6096	1.2698	2.0356	0.2570	**0.0013**
[15 10 30]	0.7588	0.6158	0.7150	**0.0076**	0.0172
[15 2 90]	0.1180	0.8928	0.6030	0.0072	**0.0007**
[30 2 30]	0.3981	0.3155	0.7800	0.0089	**0.0018**

Table 4

Average MSE and KL distances for year one reference and year two subject images.

	HM	WMP	UPL	MI	M2
MSE	20.15	**17.82**	18.97	47.38	18.59
KL	0.0542	0.509	0.1036	0.2765	**0.0403**